CHAPTER 1

INTRODUCTION

1.1 Background

Nanocomposite materials are of great interest because of their potential use in a variety of fields, such as catalysis, optics, magnetism and electronics. The properties of a nanocomposite are strongly dependent on its microstructure, not only in terms of dispersion, size distribution of the metal or metal oxide nanoparticles and features of the matrix support, but also as a function of possible interactions that might take place between nanoparticles and the matrix [1].

ZnO has been a steady point of attraction for many researchers due to its eccentric properties, such as wide band gap (3.37 eV), large exciton binding energy of 60 MeV, non-toxicity, good electrical, optical and piezoelectric behavior, and relatively low cost [2,3]. ZnO has generated great interest for its potential applications in various fields, including short-wavelength light-emitting diode and room temperature ultraviolet (UV) lasing diode, solar cell, UV-absorber, transparent conductor, field emission display, varistor and transducer, catalyst and gas sensor, etc. [2-4]. Recently, ZnO-based nanocomposites are of considerable interest in ceramics technology for applications as varistors, sensor elements and photoluminescent materials [1,5]. MgO was chosen to composite with ZnO due to MgO has a band gap of about 6.7 eV. For the purpose of changing the electrical and optical properties of ZnO, MgO was often doped into or combined with ZnO with various ways [6].

Flame spray pyrolysis (FSP) is a promising technique for the synthesis of high purity nano-sized materials with controllable size and crystallinity in a single step. It was systematically investigated using an external-mixing gas-assisted atomizer supported by six premixed methane–oxygen flamelets [7,8]. Moreover at low oxidant flow rates the specific surface area increased with increasing oxidant flow rate as the spray flame length was reduced leading to shorter residence time allowing less time for particle growth. Using oxygen as an oxidant the droplets burn much faster than in air, thus product particles experience longer residence times at higher temperature causing lower specific surface area. Therefore the specific surface area of the nanocomposites can be controlled by adjusting the oxidant flow rates. After evaporation and combustion of precursor droplets, nanocomposites were formed by nucleation, condensation, coagulation and coalescence. Thus, it is interesting to apply FSP for the production of ZnO/MgO nanocomposites. In this work, ZnO/MgO nanocomposites were further characterized by using X-ray diffraction (XRD), nitrogen adsorption (BET) analysis, scanning electron microscopy (SEM) and transmittion electron microscopy (TEM).

1.2 Zinc Oxide (ZnO) [9-13]

ZnO is a direct band gap semiconductor with E_b = 3.2 eV. The band gap of ZnO can be tuned via divalent substitution on the cation site. Substituting Mg on Zn site in epitaxial can increase the band gap to approximately 4.0 eV. ZnO normally forms in the hexagonal (wurtzite) crystal structure with a = 3.25 Å and c = 5.12 Å (Figure 1.1). The Zn atoms are tetrahedrally coordinated to four O atoms, where the Zn d-electrons hybridize with the O p-electrons. Layers occupied by zinc atoms alternate with layers occupied by oxygen atoms. Electron doping in nominally undoped ZnO has been attributed to Zn interstitials, oxygen vacancies, or hydrogen. The intrinsic defect levels that lead to n-type doping lie approximately 0.01-0.05 eV below the conduction band. The optical properties of ZnO, studied using photoluminescence, photoconductivity, and absorption reflect the intrinsic direct band gap, a strongly bound exciton state, and gap states arising from point defects. A strong room temperature, near-band-edge UV photoluminescence peak at ~3.2 eV is attributed to an exciton state, as the exciton binding energy is on the order of 60 meV. Furthermore, visible emission is also observed due to defect states. A blue-green emission, centered at around 500 nm in wavelength, has been explained within the context of transitions involving self activated centers formed by a doubly ionized zinc vacancy and an ionized interstitial Zn^+, oxygen vacancies, donor-acceptor pair recombination involving an impurity acceptor, and/or interstitial O. A broad orange-red photoluminescence emission at ~1.9 eV can be observed in some materials and has been assigned to defect states as well.

The basic materials parameters of ZnO are shown in Table 1.1 [9]. To realize any type of device technology, it is important to have control over the concentration of intentionally introduced impurities, called dopants, which are responsible for the electrical properties of ZnO. The dopants determine whether the current (and, ultimately, the information processed by the device) is carried by electrons or holes.

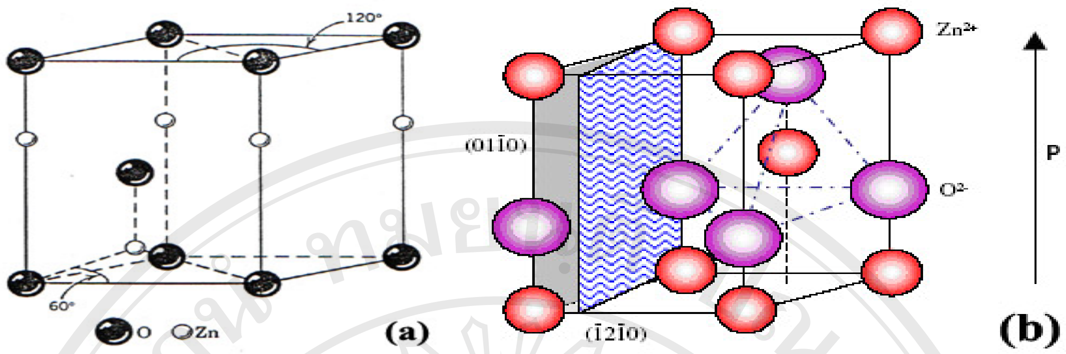

Figure 1.1 (a) Unit cell of the wurtzite structure and (b) the ZnO wurtzite structure model.

Table 1.1 Properties of wurtzite ZnO [9]

Property	**Value**
Lattice parameters at 300 K: a_o c_o a_o/c_o u	 0.32495 nm 0.52069 nm 1.602 (1.633 for ideal hexagonal structure) 0.345
Density	5.606 g/cm^3
Stable phase at 300 K	wurtzite
Malting point	1975 ^{o}C
Thermal conductivity	0.6, 1-1.2
Linear expansion coefficient (/^{o}C)	a_o: 6.5 x 10^{-6}, c_o: 3.0 x 10^{-6}
Static dielectric constant	8.656
Refractive index	2.008, 2.029
Energy gap	3.4 eV (direct)
Intrinsic carrier concentration	< 10^6 /cm^3
Exciton binding energy	60 meV
Electron effective mass	0.24
Electron Hall mobility at 300 K for low *n*-type conductivity	200 cm^2/V.s
Hole effective mass	0.59
Hole Hall mobility at 300 K for low *p*-type conductivity	5.50 cm^2/V.s

In semiconducting oxides, it is generally possible to achieve one or another type of current conductively either electrons or holes, but not both. The dopants are also called shallow level impurities because they introduce energy levels close to one of the allowed energy bands in the material and are easily ionized as a result. There may also be unintentional impurities introduced during the growth of ZnO that have a deleterious effect on the properties of the material. These are called deep level defects or impurities and may be either elemental impurities arising from contamination of the growth environment or structural defects in the ZnO crystal lattice. These structural defects can be vacancies in the crystal structure or interstitials, i.e. atoms sitting in the open regions around lattice sites. These effects may introduce energy levels deep within the forbidden band gap of ZnO and act as traps for carriers in the material. The uncontrolled defects make it very difficult to obtain the reproducible device performance and reliability.

1.3 Magnesium Oxide (MgO) [14-16]

MgO has been attractive for both fundamental and applicational research areas, because it is a very important metal oxide for use in catalysis and toxic waste remediation, and it is also used as an additive in refractory, paint and semiconductor products.

MgO is a highly ionic crystalline solid, which crystallizes into a rock salt structure (Figure 1.2). It has fcc Mg^+ and O^- sublattices, and low energy neutral (100) cleavage planes. The lattice constant of MgO is 0.421 nm and its refractive index and dielectric constant are 1.736 and 10 respectively. Magnesium oxide seems to be a good candidate for doping which regarding to its bulk properties: large band gap

(7.8 eV), high thermal conductivity and stability and an alternative dielectric to silicon dioxide (SiO_2) to reduce the electric field in capacitive networks. MgO, widely used as a substrate for high-temperature superconductor films deposition, has attracted much attention due to its low dielectric constant, low dielectric loss, and less mismatch with YBCO films. With a low dielectric loss, MgO shows a wide application in microwave devices. Due to its low refractive index, MgO is especially a suitable buffer for epitaxial optical waveguide films. Ceramic or metal/alloy oxide films are of scientific and technological importance due to their applications in optical and electronic devices, in catalytic reaction, as protective coating on metals, as single tunnel barrier and in gas sensors. They are mostly preferred due to their wide band gap and its intertness against many chemical reactions. The chemical and physical properties of palladium are shown in Table1.2

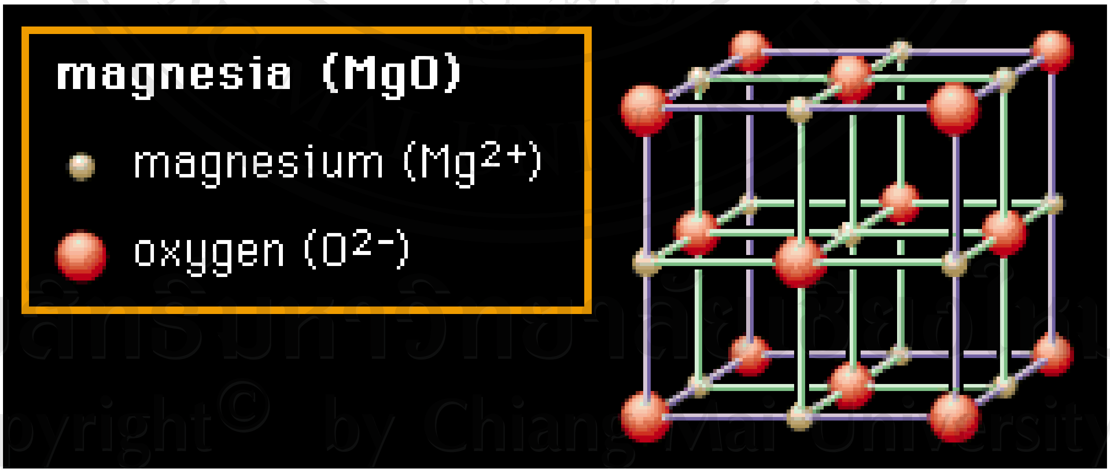

Figure 1.2 MgO rock salt structure model.

Table 1.2 Chemical and physical properties of magnesium oxide [16]

Property	**Value**
IUPAC name	Magnesium oxide
Other names	Magnesia
Physical state	White powder
Structure	Cubic
Molecular mass	40.3044 g/mol
Density	3.58 g.cm^{-3}
Melting point	2800 °C
Boiling point	3600 °C
Soluble in water	0.0086 g/100 mL
pH	10.3
Vapor density	1.39

1.4 Powder preparation

1.4.1 Sol-gel method [17,18]

The sol-gel process allows synthesizing ceramic materials of high purity and homogeneity by mean of preparation techniques different from the traditional process of fusion of oxides. This process occurs in liquid solution of organometallic precursors which, by means of hydrolysis and condensation reactions, lead to the formation of a new phase (sol). The reaction schemes were described by reaction (1.1)-(1.3)

$$\text{M-O-R} + H_2O \rightarrow \text{M-OH} + \text{R-OH (hydrolysis)} \qquad (1.1)$$

$$\text{M-OH} + \text{HO-M} \rightarrow \text{M-O-M} + H_2O \text{ (water condensation)} \qquad (1.2)$$

$$\text{M-O-R} + \text{HO-M} \rightarrow \text{M-O-M} + \text{R-OH (alcohol condensation)} \qquad (1.3)$$

The sol is made of solid particles of diameter of few hundreds nm suspended in a liquid phase. Then the particles condense in a new phase (gel) in which a solid macromolecule is immersed in a liquid phase (solvent). Drying the gel by means of low temperature treatments (25-100^{o}C), it is possible to obtain porous solid matrices.

The fundamental property of the sol-gel process is that it is possible to generate ceramic material at a temperature close to room temperature. Therefore such a procedure opened the possibility of incorporating in these glasses soft dopants, such as fluorescent dye molecules and organic chromophores into ceramic substrates.

1.4.2 Precipitation method [19-21]

The precipitation process usually follows by adjusting pH, adds chemicals to facilitate stimulate precipitation, or coagulants, and mixes the fluid in a device called a flocculator. The chemical precipitants, coagulants, and flocculants are all used to increase the particle size through aggregation. The commonly used precipitants include carbonates, sulfates, sulfides, lime and other hydroxides. The precipitants generate very fine particles that are held in suspension. Coagulants are often added to aggregate the suspended particles. Mixing in a flocculator following the addition of coagulants promotes contact between the particles, which in turn promotes particle growth and settling.

1.4.3 Hydrothermal method [22-24]

The original hydrothermal method involves heating the reaction in a closed vessel (an autoclave) with water. In a closed vessel the pressure increases and the water remains liquid above its normal boiling temperature of 100^{o}C. These conditions, in which the temperature is raised above boiling temperature of water and the pressure raised above atmosphere pressure, are known as hydrothermal conditions. Powders prepared via hydrothermal method are often unagglomerated, anhydrous and crystalline. Consequently, the prepared powders do not have to be calcined or milled. They remain unagglomerated and substantially free of impurities.

Hydrothermal synthesis offers a potentially superior technique for low cost and low temperature production of piezoelectric materials. Normally, hydrothermal synthesis has been used for preparing ceramic powders for a variety of applications. It has superiority over the other powder preparation methods in that high calcinations temperature is not necessary for the synthesis of crystallized ceramic powders.

1.4.4 Thermal decomposition method [25-27]

Thermal decomposition is defined as a chemical reaction whereby a chemical substance breaks up into at least two chemical substances when heated. It is usually an endothermic reaction as heat is required to break chemical bonds in the compound undergoing decomposition. *Thermolysis* (from *thermo-* meaning heat and -lysis meaning break down) is a chemical process by which a substance is decomposed into other substances by use of heat. The decomposition temperature of a substance is the temperature at which the substance decomposes into smaller substances or into its constituent atoms. High temperatures can also induce polymerization, which produces larger molecules, possibly also causing thermal decomposition and evaporation of smaller molecules in the process.

1.4.5 Impregnation mathod [28,29]

Impregnation method is considered as a simple method of making a catalyst. The powder of catalyst is contacted with a solution then dried and calcined. The impregnation technique requires less equipment since the filtering and forming steps are eliminated and washing may not require. It is a preferred method in preparing metal ions coating on surface of semiconductors such as TiO_2, ZnO, and SnO_2 due to its simplicity.

1.4.6 Flame spray pyrolysis [30-35]

Flame aerosol technology is the important key process for large-scale production of nano-structured materials such as carbon blacks, fumed SiO_2 and TiO_2 and to a lesser extent, for specialty chemicals such as Al_2O_3 and ZnO powders. Flame aerosol synthesis is a cost-effective and versatile process for controlled production of nanoparticles. Flame spray pyrolysis (FSP) process was systematically investigated using an external-mixing gas-assisted atomizer supported by premixed methane and oxygen flamelets [32, 33]. In flame reactors, the energy of flame is used to drive chemical reactions of precursors resulting in clusters which further grow to nanoparticles by surface growth and/or coagulation and coalescence at high temperature. The advantage of FSP include the ability to dissolve the precursor directly in the fuel, simplicity of introduction of the precursor into the hot reaction zone (e.g. a flame), and flexibility in using the high-velocity spray jet for rapid quenching of aerosol formation. In general, a flame is used to force chemical reactions of precursor compounds, finally resulting in the formation of clusters, which increase their size to a range of some nanometers by coagulation and sintering. Finally, the nanostructured powders are collected on a filter [32, 33]. The more fuel introduced the higher the flame is and due to the residence time of particles in the flame is also increased. As a consequence time for particle growth is prolonged the bigger particles are formed. External electric field reduces the average particle size in a narrow range up to a factor of two. Electric fields can be used in application as control devices. Moreover, at low oxidant flow rates, the specific surface area increased with increasing oxidant flow rate as the spray flame length was reduced, leading to shorter resident time and allowing less time for particle growth. Using pure oxygen as oxidant the droplets burn much faster than with air, thus, product particles experience longer resident times at higher temperature [31-35]. The effect of solution feed rate on particles specific surface area and crystalline size was also investigated [30]. The solution feed rate increased the flame height, and therefore coalescence was enhanced, resulting in large primary particles [30].

1.5 Characterization techniques

1.5.1 X-ray diffraction method [36-38]

X-ray diffraction is a convenient method to identify an unknown specimen by determining its crystal structure and comparing it with a repository of standard powder diffraction patterns. Exact matching of the interplanar spacings (*d values*) and intensities of all peaks between the standard and an observed diffraction patterns confirms the identity of the unknown as the same as the standard or reference material.

1.5.1.1 The advantage of X-ray diffraction method

The simplicity and advantages of the powder diffraction method for identification of an unknown substance are as follows:

- The powder diffraction pattern is determined by the exact atomic arrangement in a material, so it is like a “fingerprint” of the material.
- Each substance in a mixture produces its own characteristic diffraction pattern independently of the others.
- The X-ray diffraction pattern discloses the presence of a substance as that substance actually exists in the specimen.
- Only a small amount of the material is required for recording the X-ray diffraction pattern.
- The method is nondestructive.

1.5.1.2 Identification of crystal structure by XRD

The X-ray diffraction pattern is a fingerprint of any substance, it should be possible to unambiguously identify that material from its X-ray diffraction pattern. A large collection of X-ray diffraction pattern from a number of substances are available, then the unknown material can be identified by obtaining its diffraction pattern and then determining which pattern from the collection matches exactly with the library diffraction pattern. The Powder Diffraction File (PDF) organized by the Joint Committee on Powder Diffraction Standards (JCPDS), later renamed the International Centre for Diffraction Data (ICDD), and at present collections of nearly 80,000 standard diffraction patterns.

1.5.1.3 Theoretical considerations

Solid matter can be described as amorphous, which the atoms are arranged in a random way similar to the disorder found in a liquid. Glasses are amorphous materials. It can be described as crystalline, which the atoms are arranged in a regular pattern, and there is as smallest volume element that by repetition in three dimensions describes the crystal. The smallest volume element is called a unit cell. The dimension of the unit cell is described by three axes: a, b, c and the angles between them alpha, beta and gamma. About 95% of all solids can be described as crystalline.

An electron in an alternating electromagnetic field will oscillate with the same frequency as the field. When an X-ray beam hits an atom, the electrons around the atom start to oscillate with the same frequency as the incoming beam. In almost all directions will also have destructive interference, that is, the combining waves are out of phase and there is no resultant energy leaving the solid sample. However the atoms in a crystal are arranged in a regular pattern, and in a very few directions will have constructive interference. The waves will be in phase and there will be well defined X-ray beams leaving the sample at various directions. Hence, a diffracted beam may be described as a beam composed of a large number of scattered rays mutually reinforcing one another.

This model is rather complex to handle mathematically the X-ray reflections from a series of parallel planes inside the crystal. The orientation and interplanar spacings of these planes are defined by the three integers h, k, l called indices. A given set of planes with indices h, k, and l cut the a-axis of the unit cell in h sections, the b-axis in k sections and the c-axis in l sections. A zero indicates that the planes are parallel to the corresponding axis. In general, the 2, 2, 0 planes cut the a–axis and the b–axis in half, but are parallel to the c–axis as shown in Figure 1.3

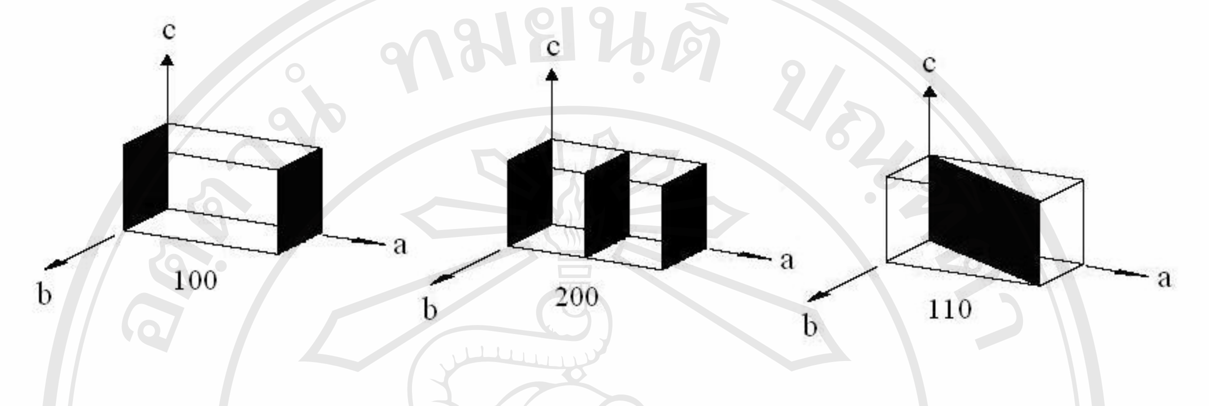

Figure 1.3 The determination of indices of plane [37]

The three dimensional diffraction grating as a mathematical model, the three indices h, k, l become the order of diffraction along the unit cell axes a, b and c respectively. It should now be clear that, depending on what mathematical model has in mind, the terms X-ray reflection and X-ray diffraction as synonyms. An X-ray beam incident on a pair of parallel planes P1 and P2, separated by an interplanar spacing d as shown in Figure 1.4.

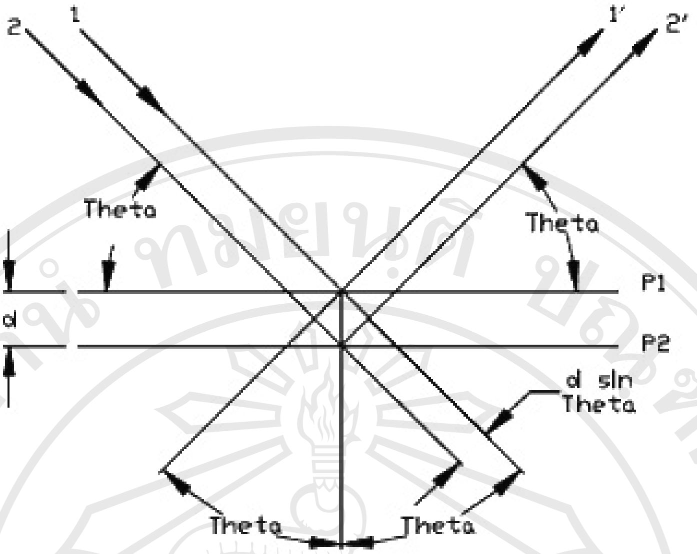

Figure1.4 Diffraction of X-ray by a crystal [37]

The two parallel incident rays 1 and 2 make an angle (θ) with these planes. A reflected beam of maximum intensity will result if the waves represented by $1'$ and $2'$ are in phase. The difference in path length between1 to $1'$ and 2 to $2'$ must then be an integral number of wavelengths, (λ). The relationship mathematically in Bragg's law is shown in equation 1.4.

$$\mathbf{2d\sin\theta = n\lambda} \tag{1.4}$$

The process of reflection is described here in terms of incident and reflected (or diffracted) rays, each making an angle θ with a fixed crystal plane. Reflections occur from planes set at angle θ with respect to the incident beam and generates a reflected beam at an angle 2θ from the incident beam. The possible d-spacing defined by the indices h, k, l are determined by the shape of the unit cell. Rewriting Bragg's law is shown in equation 1.5:

$$\mathbf{\sin\theta = \lambda/2d} \tag{1.5}$$

Therefore the possible 2θ values where reflections are determined by the unit cell dimensions. However, the intensities of the reflections are determined by the distribution of the electrons in the unit cell. The highest electron density is found around atoms. The intensities depend on what kind of atoms exists and where in the unit cell of atoms are located. Planes going through areas with high electron density will reflect strongly, planes with low electron density will give weak intensities.

1.5.1.4 Particle size measurement by XRD

For good quality crystalline material of dimension 0.1 nm is made up of approximately 1,000,000 crystal planes (assuming that d_{hkl} = 1 nm). When an X-ray collides with these planes close to the Bragg angle, diffraction intensity is not observed because the X-rays reflected from the multitude of parallel planes annihilate one another. With such materials diffraction peaks are produced only within a very narrow window very close to the Bragg angle. Particle sizes are often in the range 1-100 nm for heterogeneous catalysts. In such circumstances the number of stacked planes per particle is in the range of 5-100. This results in the broadening of the XRD peaks because there are insufficient reflecting planes to annihilate phase reflection at angle that are fairly far and removed from the Bragg angle.

This effect has been quantified as the Scherrer equation:

$$t_{\mathrm{hkl}} = K\lambda / B_{\mathrm{hkl}} \cos\theta_{\mathrm{hkl}} \tag{1.6}$$

Where:

t_{hkl} is the particle size measured from X-rays diffracted from the (*hkl*) planes

B_{hkl} is the full-width at half-maximum (FWHM) of the peak measured in radian from the (*hkl*) planes

θ_{hkl} is the Bragg angle for the reflection from the (*hkl*) planes

K is a constant which depends to some extent on the particles shape. For spherical particles $K = 0.9$.

Figure 1.5 demonstrates how particle size and shape can be determined by XRD analysis. A sample was analyzed by XRD and exhibited the pattern shown, namely one very narrow line and another rather broad. In this case the apparent conflict is caused by the shape of particle. X-rays reflected from the (100) planes, a large particle and a narrow line results. X-rays reflected from the (001) planes, a small particle and a broad line results.

When measuring particles size using XRD line broadening it is important to realize that not all the broadening is due to the particle size effect. Near perfect crystals should produce extremely narrow XRD lines, but even here some broadening occurs because of instrumental factors. Instrumental contribution to line broadening should be subtracted out by running the XRD of a good quality polycrystalline sample versus the same materials.

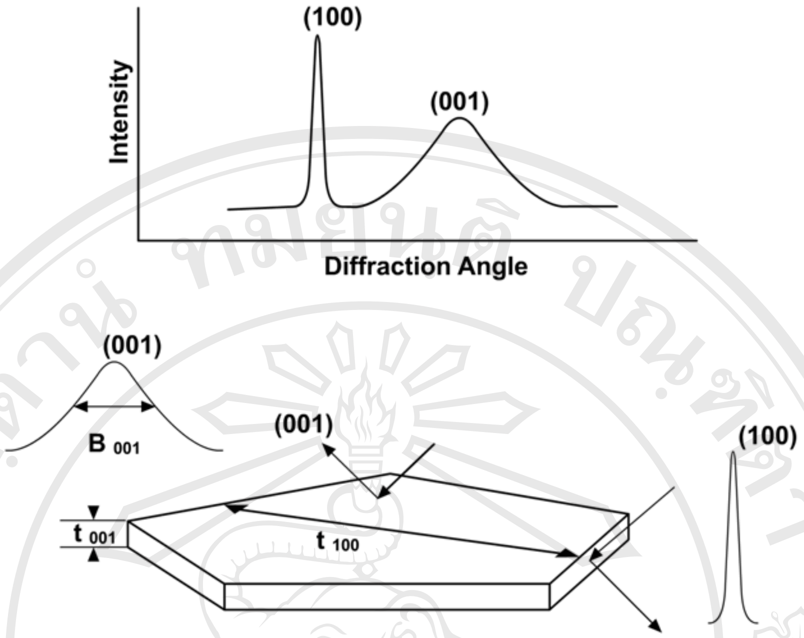

Figure 1.5 Schematic diagram of X-ray line broadening effects [38]

1.5.1.5 Sample preparation

In X-ray diffraction work, normally distinguishes between single crystal and polycrystalline or in powder applications. The single crystal sample is a perfect (all unit cells aligned in a perfect extended pattern) crystal with a cross section of about 0.3 mm. The single crystal diffractometer and associated computer package is used mainly to elucidate the molecular structure of novel compounds, either natural products or man made molecules. Powder diffraction is mainly used for “finger print identification” of various solid materials, e.g. asbestos, quartz.

In powder or polycrystalline diffraction it is important to have a sample with a smooth plane surface. If possible, grinding the sample was normally performed down to particles of about 0.002 mm to 0.005 mm in cross section. The ideal sample is homogeneous and the crystallites are randomly distributed (problems which will occur if the specimen deviates from this ideal state will be pointed out later). The sample is pressed into a sample holder so that a smooth flat surface is obtained. Ideally, it should be a random distribution of all possible h, k, l planes. Only crystallites having reflecting planes (h, k, l) parallel to the specimen surface will contribute to the reflected intensities. In a truly random sample, each possible reflection from a given set of h, k, l planes will have an equal number of crystallites contributing to it. The sample needs to be fixed through the glancing angle θ in order to produce all possible reflections.

1.5.2 Scanning Electron Microscopy (SEM) [39-41]

The scanning electron microscope (SEM) is a type of electron microscope that creates various images by focusing a high energy beam of electrons onto the surface of a sample and detecting signals from the interaction of the incident electrons with the sample's surface. The type of signals gathered in an SEM varies and can include secondary electrons, characteristic X-rays, and back scattered electrons. In an SEM these signals come not only from the primary beam impinging upon the sample, but from other interactions within the sample near the surface. The SEM is capable of producing high-resolution images of a sample surface in its primary use mode, secondary electron imaging. Due to the manner in which this image is created, SEM images have great depth of field yielding a characteristic three-dimensional appearance useful for understanding the surface structure of a sample. This great depth of field and the wide range of magnifications are the most familiar imaging mode for specimens in the SEM. Characteristic X-rays are emitted when the primary beam causes the ejection of inner shell electrons from the sample and are used to tell the elemental composition of the sample. The back-scattered electrons emitted from the sample may be used alone to form an image or in conjunction with the characteristic X-rays as atomic number contrast clues to the elemental composition of the sample as shown in Figure 1.6.

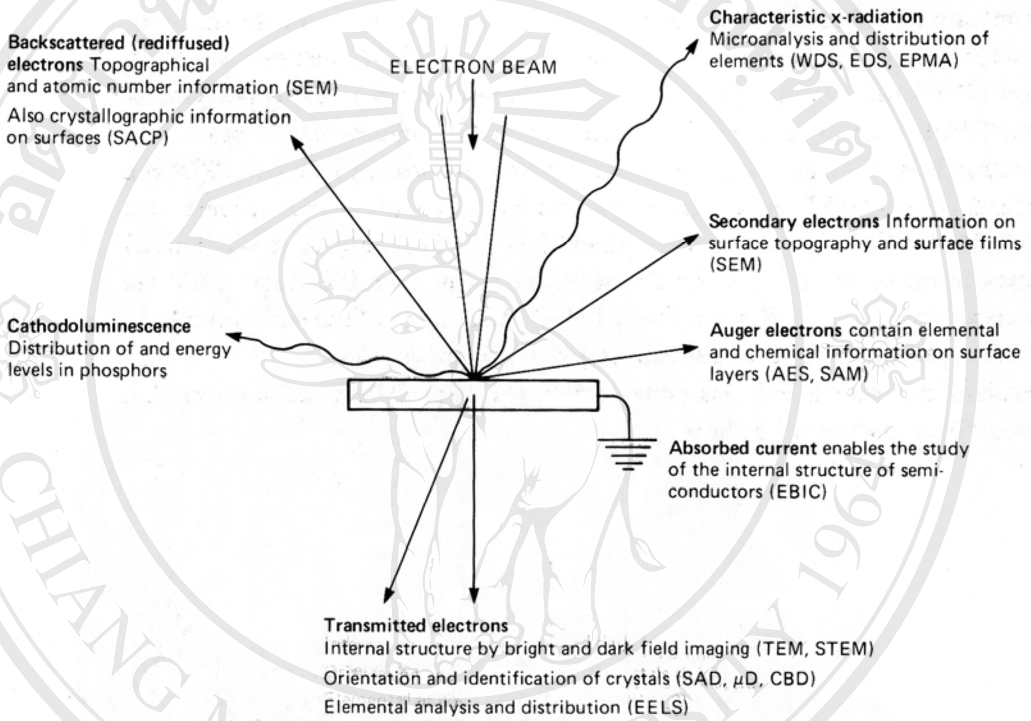

Figure 1.6 Schematic representation of the information resulting from the interaction between the electron beam and the specimen in an electron microscope [39]

1.5.2.1 Detection of secondary electrons

The most common imaging mode monitors low energy (<50 eV) is secondary electrons. Due to their low energy, these electrons originate within a few nanometers from the surface. The electrons are detected by an Everhart-Thornley detector which is a typical of scintillator-photomultiplier device and the resulting signal is rendered into a two-dimensional intensity distribution that can be viewed and saved as a digital image. This process relies on a faster-scanned primary beam. The brightness of the signal depends on the number of secondary electrons reaching the detector. If the beam enters the sample perpendicular to the surface, then the activated region is uniform about the axis of the beam and a certain number of electrons "escape" from within the sample. As the angle of incidence increases, the "escape" distance of one side of the beam will decrease, and more secondary electrons will be emitted. Thus steep surfaces and edges tend to be brighter than flat surfaces, which results in images with a well-defined, three-dimensional appearance. Using this technique, resolutions less than 1 nm are possible.

1.5.2.2 Detection of backscattered electrons

Backscattered electrons (BSE) consist of high-energy electrons originating in the electron beam that are reflected or back-scattered out of the specimen interaction volume. Backscattered electrons may be used to detect contrast between areas with different chemical compositions, especially when the average atomic number of the various regions is different, since the brightness of the BSE image tends to increase with the atomic number.

Backscattered electrons can also be used to form an electron backscatter diffraction (EBSD) image. This image can be used to determine the crystallographic structure of the specimen.

There are fewer backscattered electrons emitted from a sample than secondary electrons. The number of backscattered electrons leaving the sample surface upward might be significantly lower than those that follow trajectories toward the sides.

Additionally, in contrast with the case with secondary electrons, the collection efficiency of backscattered electrons cannot be significantly improved by a positive bias common on Everhart-Thornley detectors. This detector positioned on one side of the sample and has low collection efficiency for backscattered electrons due to small acceptance angles. The use of a dedicated backscattered electron detector above the sample in a "doughnut" type arrangement, with the electron beam passing through the hole of the doughnut, greatly increases the solid angle of collection and allows for the detection of more backscattered electrons.

1.5.2.3 Beam-injection analysis of semiconductors

The nature of the SEM's probe, energetic electrons, makes it uniquely suited to examining the optical and electronic properties of semiconductor materials. The high-energy electrons from the SEM beam will inject charge carriers into the semiconductor. Thus, beam electrons lose energy by promoting electrons from the valence band into the conduction band, leaving behind the holes.

In a direct band gap material, recombination of these electron-hole pairs will result in cathodoluminescence; if the sample contains an internal electric field, such as is present at a p-n junction, the SEM beam injection of carriers will cause electron beam induced current (EBIC) to flow.

Cathodoluminescence and EBIC are referred to as "beam-injection" techniques, and are very powerful probes of the optoelectronic behavior of semiconductors, particularly for studying nanoscale features and defects.

1.5.2.4 Cathodoluminescence

Cathodoluminescence (CL), the emission of light when atoms excited by high-energy electrons return to their ground state, is analogous to UV-induced fluorescence, and some materials such as zinc sulphide and some fluorescent dyes, exhibit both phenomena. Cathodoluminescence is most commonly experienced in everyday life as the light emission from the inner surface of the cathode ray tube (CRT) in television sets and computer CRT monitors. In the SEM, CL detectors either collect all light emitted by the specimen, or can analyse the wavelengths emitted by the specimen and display a spectrum or an image of the cathodoluminescence in real colour.

1.5.2.5 X-ray microanalysis

X-rays, which are also produced by the interaction of electrons with the sample, may also be detected in an SEM equipped for energy-dispersive X-ray spectroscopy or wavelength in dispersive X-ray spectroscopy.

1.5.2.6 Resolution of the SEM

The spatial resolution of the SEM depends on the size of the electron spot, which in turn depends on both the wavelength of the electrons and the magnetic electron-optical system which produces the scanning beam. The resolution is also limited by the size of the interaction volume, or the extent to which the material interacts with the electron beam. The spot size and the interaction volume both might be large compared to the distances between atoms, so the resolution of the SEM is not high enough to image individual atoms, as is possible in the shorter wavelength (i.e.

higher energy) transmission electron microscope (TEM). The SEM has compensating advantages, though, including the ability to image a comparatively large area of the specimen; the ability to image bulk materials (not just thin films or foils); and the variety of analytical modes available for measuring the composition and nature of the specimen. Depending on the instrument, the resolution can fall somewhere between less than 1 nm and 20 nm. In general, SEM images are easier to interpret than TEM images.

1.5.2.7 Procedure

Figure 1.7 shows the schematic diagram of a scanning electron microscope. A detailed explanation of how a typical SEM functions are as follows:

1) The "Virtual Source" at the top represents the electron gun, producing a stream of monochromatic electrons.
2) The stream is condensed by the first condenser lens (usually controlled by the "coarse probe current knob"). This lens is used to both form the beam and limit the amount of current in the beam. It works in conjunction with the condenser aperture to eliminate the high-angle electrons from the beam
3) The beam is then constricted by the condenser aperture (usually not user selectable), eliminating some high-angle electrons
4) The second condenser lens forms the electrons into a thin, tight, coherent beam and is usually controlled by the "fine probe current knob"
5) A user selectable objective aperture further eliminates high-angle electrons from the beam

6) A set of coils then "scan" or "sweep" the beam in a grid fashion (like a television), dwelling on points for a period of time determined by the scan speed (usually in the microsecond range)
7) The final lens, the Objective, focuses the scanning beam onto the part of the specimen desired.
8) When the beam strikes the sample (and dwells for a few microseconds) interactions occur inside the sample and are detected with various instruments
9) Before the beam moves to its next dwell point these instruments count the number of interactions and display a pixel on a CRT whose intensity is determined by this number (the more reactions the brighter the pixel).
10) This process is repeated until the grid scan is finished and then repeated, the entire pattern can be scanned 30 times per second.

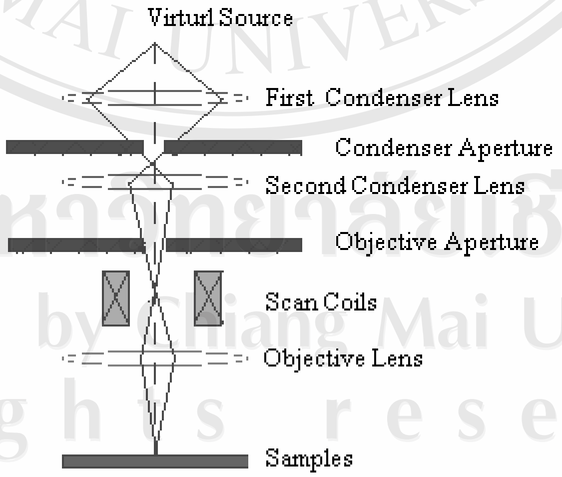

Figure 1.7 Schematic diagram of a scanning electron microscope [41]

1.5.3 Transmission Electron Microscopy (TEM) [39, 42-44]

The TEM is used heavily in both material science/metallurgy and the biological sciences. In both cases the specimens must be very thin and able to withstand the high vacuum present inside the instrument.

For biological specimens, the maximum specimen thickness is roughly 1 micrometre. To withstand the instrument vacuum, biological specimens are typically held at liquid nitrogen temperatures after embedding in vitreous ice, or fixated using a negative staining material such as uranyl acetate or by plastic embedding. Typical biological applications include tomographic reconstructions of small cells or thin sections of larger cells and 3-D reconstructions of individual molecules via Single Particle Reconstruction.

In material science/metallurgy the specimens tend to be naturally resistant to vacuum, but must be prepared as a thin foil, or etched so some portion of the specimen is thin enough for the beam to penetrate. Preparation techniques to obtain an electron transparent region include ion beam milling and wedge polishing. The focused ion beam (FIB) is a relatively new technique to prepare thin samples for TEM examination from larger specimens. Because the FIB can be used to micro-machine samples very precisely, it is possible to mill very thin membranes from a specific area of a sample, such as a semiconductor or metal. Materials that have dimensions small enough to be electron transparent, such as powders or nanotubes, can be quickly produced by the deposition of a dilute sample containing the specimen onto support grids. The suspension is normally in a volatile solvent, such as ethanol, ensuring that the solvent rapidly evaporates allowing a sample that can be rapidly analysed.

The imaging techniques explained below are particularly important in materials science. Faults in crystals affect both the mechanical and the electronic properties of materials, so understanding how they behave gives a powerful insight. By carefully selecting the orientation of the sample, it is possible not just to determine the position of defects but also to determine the type of defect present. If the sample is orientated so that one particular plane is only slightly tilted away from the strongest diffracting angle (known as the Bragg Angle), any distortion of the crystal plane that locally tilts the plane to the Bragg angle will produce particularly strong contrast variations. However, defects that produce only displacement of atoms that do not tilt the crystal to the Bragg angle (i.e. displacements parallel to the crystal plane) will not produce strong contrast.

Furthermore, the high resolution TEM (HRTEM) technique allows the direct observation of crystal structure and therefore has an advantage over other methods in that there is no displacement between the location of a defect and the contrast variation caused in the image. However, it is not always possible to interpret the lattice images directly in terms of sample structure or composition. This is because the image is sensitive to a number of factors (specimen thickness and orientation, objective lens defocus, spherical and chromatic aberration), and although quantitative interpretation of the contrast shown in lattice images is possible, it is inherently complicated and may require extensive simulation of the images. Computer modeling of these images has added a new layer of understanding to the study of crystalline materials.

1.5.3.1 Imaging in the TEM

The contrast in a TEM image is not like the contrast in a light microscope image. A crystalline material interacts with the electron beam mostly by diffraction rather than absorption, although the intensity of the transmitted beam is still affected by the volume and density of the material through which it passes. The intensity of the diffraction depends on the orientation of the planes of atoms in a crystal relative to the electron beam; at certain angles the electron beam is diffracted strongly from the axis of the incoming beam, while at other angles the beam is largely transmitted. Modern TEMs are often equipped with specimen holders that allow the user to tilt the specimen to a range of angles in order to obtain specific diffraction conditions, and apertures placed below the specimen allow the user to select electrons diffracted in a particular direction.

A high-contrast image can therefore be formed by blocking electrons deflected away from the optical axis of the microscope by placing the aperture to allow only unscattered electrons through. This produces a variation in the electron intensity that reveals information on the crystal structure, and can be viewed on a fluorescent screen, or recorded on photographic film or captured electronically.

This technique (known as Bright Field or Light Field) is particularly sensitive to extended crystal lattice defects in an otherwise ordered crystal, such as dislocations. As the local distortion of the crystal around the defect changes the angle of the crystal plane, the intensity of the scattering will vary around the defect. As the image is formed by the distortion of the crystal planes around the defect, the contrast in these images does not normally coincide exactly with the defect, but is slightly to one side.It is also possible to produce an image from electrons deflected by a particular crystal plane. By either moving the aperture to the position of the deflected electrons, or tilting the electron beam so that the deflected electrons pass through the centred aperture, an image can be formed of only deflected electrons, known as a Dark Field image.

In the most powerful diffraction contrast TEM instruments, crystal structure can also be investigated by High Resolution Transmission Electron Microscopy (HRTEM), also known as phase contrast imaging as the images are formed due to the differences in phase of electron waves scattered through a thin specimen.

Resolution of the HRTEM is limited by spherical and chromatic aberration, but a new generation of aberration correctors has been able to overcome spherical aberration. Software correction of spherical aberration has allowed the production of images with sufficient resolution to show carbon atoms in diamond separated by only 0.89 ångströms (89 pm, one ångström is 10^{-10} m of a meter or 100 picometers) and atoms in silicon at 0.78 ångströms (78 pm) at magnifications of 50 million times. Improved resolution has also allowed the imaging of lighter atoms that scatter electrons less efficiently. The ability to determine the positions of atoms within materials has made the HRTEM an indispensable tool for nanotechnology research and development in many other fields, including heterogeneous catalysis and the development of semiconductor devices for electronics and photonics.

1.5.3.2 Diffraction

In conventional electron diffraction the region of interest is selected by means of a physical aperture. The smallest area which can be selected by this technique is limited by the spherical aberration of the objective lens and is usually about 1 μm in diameter. By using the small probes obtainable either in ‘nanoprobe’ or scanning modes it is possible to select a smaller area of the specimen with the focused beam. This will give, depending on the convergence angle set by the condenser aperture, a micro-selected area diffraction pattern or a convergent beam diffraction pattern as shown in Figure 1.8 (a), (b).

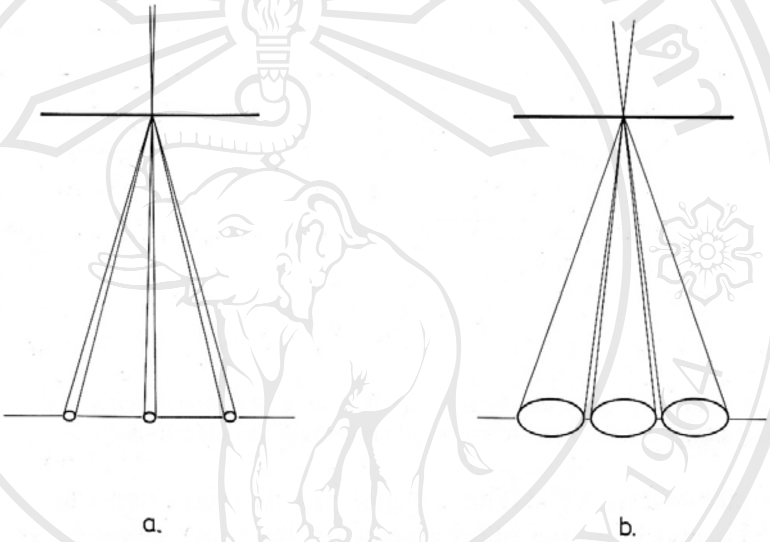

Figure 1.8 The approximate geometry of (a) microdiffraction and (b) convergent beam diffraction [42]

1.5.3.3 Analysis

The two techniques of energy dispersive X-ray analysis (EDX) and electron energy loss analysis (EELS) are frequently available on TEM/STEM instruments. The first uses characteristic X-rays excited from the small volume of specimen irradiated by the beam, while the second detects the energy lost by electrons which have interacted with the specimen. The EDX detector is fitted to the side of the microscope close to the specimen, whereas the EELS spectrometer sits of the microscope close to the specimen. Both types of analysis are useful and be able to define the analyzed region by focusing the beam onto a very small area using ‘nanoprobe’ or scanning modes.

1.5.3.4 Procedure

Figure 1.9 shows the schematic diagram of transmission electron microscope. The detailed explanation of how TEM functions are as follows:

1. The "Virtual Source" at the top represents the electron gun, producing a stream of monochromatic electrons.
2. This stream is focused to a small, thin, coherent beam by the use of condenser lenses 1 and 2. The first lens (usually controlled by the "spot size knob") largely determines the "spot size"; the general size range of the final spot that strikes the sample. The second lens (usually controlled by the "intensity or brightness knob" actually changes the size of the spot on the sample; changing it from a wide dispersed spot to a pinpoint beam.
3. The beam is restricted by the condenser aperture (usually user selectable), knocking out high angle electrons (those far from the optic axis, the dotted line down the center)
4. The beam strikes the specimen and parts of it are transmitted
5. This transmitted portion is focused by the objective lens into an image
6. Optional Objective and Selected Area metal apertures can restrict the beam; the Objective aperture enhancing contrast by blocking

out high-angle diffracted electrons, the Selected Area aperture enabling the user to examine the periodic diffraction of electrons by ordered arrangements of atoms in the sample

7. The image is passed down the column through the intermediate and projector lenses, being enlarged all the way
8. The image strikes the phosphor image screen and light is generated, allowing the user to see the image. The darker areas of the image represent those areas of the sample that fewer electrons were transmitted through (they are thicker or denser). The lighter areas of the image represent those areas of the sample that more electrons were transmitted through (they are thinner or less dense)

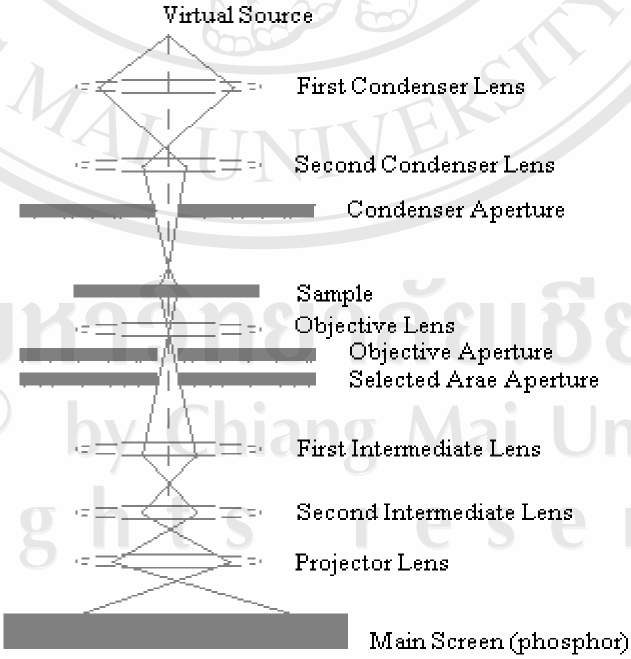

Figure 1.9 Schematic diagram of a transmission electron microscope [43]

1.5.4 The Brunauer-Emmett-Teller (BET) [45,46]

BET theory is a well-known rule for the physical adsorption of gas molecules on a solid surface. In 1938, Stephen Brunauer, Paul Hugh Emmett, and Edward Teller published an article about the BET theory in a journal for the first time; “BET” consists of the first initials of their family names.

1.5.4.1 BET theory

The Brunauer-Emmett-Teller method is base on non-specific physisorption of a gas (N_2 or Ar) onto a solid close to the condensation temperature of the adsorbing gas. Adsorption is characterized by an isotherm which represents the equilibrium amount of gas adsorbed on a solid at a given temperature as a function of pressure.

The concept of the theory is an extension of the Langmuir theory, which is a theory for monolayer molecular adsorption, to multilayer adsorption with the following hypotheses:

(a) gas molecules physically adsorb on a solid in layers infinitely

(b) there is no interaction between each adsorption layer

(c) the Langmuir theory can be applied to each layer.

The resulting BET equation is expressed by (1.7):

$$\frac{1}{V\,[(Po/P)\text{-}1]} = \frac{1}{V_mC} + \frac{C\text{-}1}{V_mC}\,\frac{P}{Po} \qquad (1.7)$$

Where:

P and P_0 are the equilibrium and the saturation pressure of adsorbates at the temperature of adsorption,

v is the adsorbed gas quantity (for example, in volume units)

v_m is the monolayer adsorbed gas quantity

c is the BET constant, which is expressed by (1.8):

$$C = \exp\left(\frac{E_1 - E_L}{RT}\right) \qquad (1.8)$$

Where:

E_1 is the heat of adsorption for the first layer

E_L is that for the second and higher layers and is equal to the heat of liquefaction.

1.5.4.2 BET plot

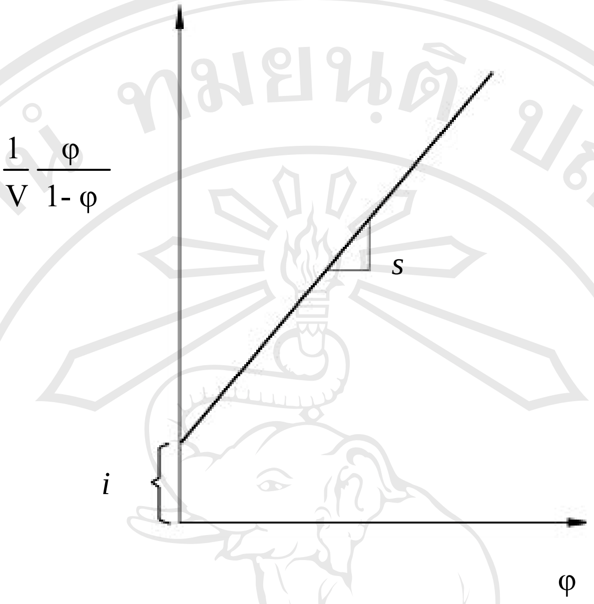

Figure 1.10 Typical BET plot [45]

Equation (1.7) is an adsorption isotherm and can be plotted as a straight line with 1 / $V[(P_0 / P) - 1]$ on the y-axis and $\varphi = P / P_0$ on the x-axis according to experimental results. This plot is called a BET plot. The linear relationship of this equation is maintained only in the range of $0.05 < P / P_0 < 0.35$. The value of the slope s and the y-intercept i of the line are used to calculate the monolayer adsorbed gas quantity V_m and the BET constant C. The following equations can be used:

$$s = \frac{C\text{-}1}{V_m C} \tag{1.9}$$

$$i = \frac{1}{V_m C} \tag{1.10}$$

Solving the preceding equations for V_m and C gives

$$Vm = \frac{1}{s+i} \tag{1.11}$$

and (1.12)

$$C = \frac{s}{i} + 1$$

1.5.4.3 Surface area calculation

The BET method is widely used in surface science for the calculation of surface areas of solids by physical adsorption of gas molecules. A total surface area S_{total} and a specific surface area S are evaluated by the following equations:

$$S_{total} = \frac{V_m \overline{N} . \mathcal{A}}{\overline{M}} \tag{1.13}$$

Where:

S_{total}	is sample surface area
$\mathcal{A}$	is the cross-sectional area
$\overline{M}$	is the molecular weight of an adsorbate molecule
$\overline{N}$	is the Avogadro’s number

1.5.4.4 Particle Size (d_{BET})

The particle size (d_{BET}) is calculated by BET measurement using specific surface area (SSA) and density of sample by assuming that the particles do have spherical shape. The following equation can be used:

$$d_{BET} = \frac{6}{SSA_{BET}\,\rho_{sample}} \qquad (1.14)$$

Where:

ρ_{sample} is the density of sample

1.6 Literature review

Yamamoto *et al.* (2000) [47] reported the antibacterial activity for MgO-ZnO solid solution by measuring the change in electrical conductivity with bacterial growth. MgO-ZnO solid solution powders were prepared by heating at 1400 ^{0}C for 3h in air. A single phase with cubic type structure was obtained in the weight ratio range (MgO/ZnO) of 4.0 and 1.5 but the ratio of 0.67 resulted in a ZnO phase in addition to solid solution. After milling the solid solution powders by planetary ball mill, the average particle size and the specific surface area of these powders became 0.1 μm and 26 m^2/g, respectively, which were used in the test of antibacterial activity. The results of antibacterial tests, the activity increased with increasing the powder concentration in the medium. Increasing the doping amount of ZnO in MgO-ZnO solid solution, it was found that a decrease in the antibacterial activity against *Escherichia coli* and *Staphylococcus aureus*. The pH value in physiological saline at the powder concentration of 2.5 mg/ml showed in the alkali region above 10.0 and decrease with the increase of ZnO amount in solid solution. The decrease in antibacterial activity, therefore, was associated with the decrease of pH value in medium.

Sawai J. (2003) [48] reported antibacterial activities of metallic oxide (ZnO, MgO and CaO) powders against *Staphylococcus aureus* and *Escherichia coli* by measuring the change in electrical conductivity of the growth medium caused by bacterial metabolism (conductimetric assay). The obtained conductivity curves were analyzed using the growth inhibition kinetic model proposed by Takahashi [49] for calorimetric evalution, and the metallic oxides were determined for the antibacterial efficacy and kinetic parameters. The parameters provided some useful indicators for antimicrobial agents, such as the dependence of antibacterial activity on agent concentration, and the affinity between the agent and the bacterial cells. CaO was the most effective, followed by MgO and ZnO, against *E. coli*. On the other hand, ZnO was the most effective for *S. aureus* and was suggested to have a strong affinity to the cells of *S. aureus.*

Seo *et al.* (2003) [50] synthesized the nanoparticles of ZnO, MgO and NiO from droplets of aqueous salt solution in the flame spray pyrolysis reactor. A conventional spray pyrolysis, in which electrical furnace reactor was used, to produce nanoparticles only from acetate precursor. If the reactor pressure was low (~60 torr), nitrate salt precursor was successfully produces nanoparticles. Nanoparticles were produced from nitrate as well as acetate salt precursor solution when propane-oxygen diffusion flame was employed to decompose the aqueous aerosol droplets. At low flame temperature, however, nanoparticles were not formed and the particle morphology was similar to the morphology produced by the conventional spray pyrolysis. At high flame temperature, nanoparticles were formed, regardling the salt type. Nanoparticles were formed at lower flame temperature from acetate salts than from nitrate salts. All nanoparticle prepared in this work were fully crystallized and the size measured from transmission electron microscopy images was around 30 nm. This size agreed well with the particle size calculated from X-ray diffraction and specific surface area measurement.

Panin *et al.* (2004) [51] prepared the optical and structural properties of mixed ZnO/MgO particles by solution techniques. The samples annealed at 400-1000 ^{0}C showed the ZnO (MgZnO) particle sizes were in the range of 10-100 nm. Annealing at high temperatures (>700^{0}C) led to Mg diffusion in ZnO and $Mg_xZn_{1-x}O$ alloy formation. The blue shifts of the near-band-edge emission as a result of the alloy band gap widening and the quantum confinement effect for small size particles were demonstrated.

Bhattacharya et al. (2004) [52] deposited $Mg_xZn_{1-x}O$ (MZO) thin films from MZO targets as well as sequential deposition of ZnO/MgO multilayers on c-plane Al_2O_3 substrates using pulsed laser deposition. The total thickness of the films was 300 nm. For multilayer deposition, the thickness of each single ZnO layer was varied in range from 0.75 to 2.5 nm followed with the MgO layer thickness of 1 nm. The transition of the hexagonal was changed to the cubic phase and was observed with increasing of Mg concentration above 40% from the single target. Similar structural change was also observed with increasing a thickness of single ZnO layer from 2.5 to 0.75 nm in multilayer deposition. The bandgap was increased with increasing the Mg contents from 3.3 to 6.2 eV as well as with the change of ZnO sublayer thickness. It had not been possible to fabricate single phase stable MZO alloys with a bandgap between 4 and 6 eV.

Panin *et al.* (2005) [53] reported the effect of thermal annealing on the structural and the optical properties of ZnO/MgO particle structures prepared by solution techniques. The results showed the wurtzite structure of ZnO nanoparticles. The particle sizes could be observed ranging from 10-100 nm as a function of annealing temperature between 400 - 600 ^{0}C The ZnO/MgO composite annealed at above 800 ^{0}C showed $Mg_xZn_{1-x}O$ alloy formation due to diffusion of the Mg atoms into ZnO nanoparticles. Cathodoluminescence (CL) spectra displayed a blue shift of the nearband-edge emission, indicative of an increase in the band gap of the $Mg_xZn_{1-x}O$ alloy and the quantum confinement effect in the small size of the particles.

Saravanamurugan *et al.* (2005) [54] reported the liquid phase of Claisen-Schmidt condensation between $2'$ -hydroxyacetophenone and benzaldehyde to form $2'$ -hydroxychalcone, followed by intramolecular cyclisation to form flavanone which was carried out over zinc oxide supported metal oxide catalysts under solvent free condition. The reaction was carried out over ZnO supported MgO, BaO, K_2O, and Na_2O catalysts with 0.2 g of each catalyst at 140 ^{0}C for 3 h. Magnesium oxide impregnated zinc oxide was observed to offer higher conversion of $2'$ -hydroxyacetophenone than other catalysts. Further MgO impregnated with various supports such as HZSM-5, Al_2O_3 and SiO_2 were also used for the reaction to assess the suitability of the support. The order of activity of the support was ZnO > SiO_2 > Al_2O_3 > HZSM-5. An optimum weight percentage of MgO loaded on ZnO for good catalytic conversion of $2'$-hydroxyacetophenone. MgO/ZnO (10wt%)

was a better catalyst than KF/ natural phosphate for the synthesis of chalcone and flavanone under solvent free conditions for 1 h reaction time.

Fu *et al.* (2006) [55] prepared ZnO/MgO nanocomposite with different MgO loading by the combustion method. The influence of the structures and photoluminescence (PL) properties on the annealing process were investigated. The nanocomposite had an ultraviolet emission property comparing to the pure ZnO nanocrystals synthesized via the same technique, and the enhancement was ascribed to the incorporation of MgO phase .The structure and PL properties of ZnO/MgO nanocomposite with MgO content of 40 mol% was investigated. The X-ray photoelectron spectroscopy (XPS) indicated the charge transfer taking place between ZnO and MgO phase by forming heterojunction-like structures, which was required by electronic equilibrium across the junction. Transmission electron microscope (TEM) observation was used to confirm the intimate contact between ZnO and MgO grains. The charge transfer results in the band bending of ZnO, changed the electronic states of the defects relating to visible band in ZnO. This mechanism was provided an effective way to modify the emission property of nanomaterials.

Ebothe *et al.* (2006) [56] reported the large effctive second-order optical susceptibility equal to about 52 pm/V for ZnO films with thickness about several μm deposited on MgO substrate by molecular epitaxial method using a bicolour coherent treatment by a pulsed 1.32 μm Nd-YAG laser and its second harmonic at k = 0.66 μm. The written grating was stable during 24 days and its optical susceptibility decreased not more than 26% with respect to the initially written one after interruption of optical treatment. The same measurements performed for the ZnO films deposited by metaloorganic chemical vapor deposition, pulsed laser ablation and spray pyrolysis were shown the output optical susceptibility to be at least half order less. The temperature dependences of the second order susceptibilities were shown that it achieved a maximum near a temperature of 261 K. Other methods did not show substantial temperature dependences. A maximal second harmonic generation signal was achieved for the films with thickness of about 2.75 μm.

Wang *et al.* (2006) [6] fabricated the ZnO/MgO multilayer thin films on Si(111) substrates by pulsed laser deposition. Compared with highly c-axis orientation ZnO films, in the multilayer films the position of (0 0 2) peak of ZnO had an excursion of 0.121 toward larger degree, and UV peak of ZnO had a blue shift of 4 nm because of the doping of Mg. The film was found to be a polycrystal grain and had more crystal direction than ZnO films. In TEM images, no single MgO phase was found and mainly composed of ZnO grain with (0 0 2) direction because most of the Mg ions doped into ZnO lattice and a small quantity of Mg ions formed primitive cubic MgO_2 instead of MgO. This was because the high oxygen pressure and high growth temperature made excessive oxygen content in the film.

Zhang *et al.* (2006) [57] synthesized the $Zn_{1-x}Mg_xO$ pellets using traditional solid-reaction method and investigated the luminescent properties. ZnO doped with MgO revealed long after glow emission that could last for more than 10 min after the samples were sintered in a sealed crucible above a certain temperature. The emission spectra of $Zn_{1-x}Mg_xO$ $(0 < x < 1)$ can be calculated using a Gaussian fit to two peaks, and the relative intensity of the two emission peaks altered with increasing the sintering temperature. The position of the two emission peaks showed slight red shift when the sintering temperature increases from 1100 to 1250^0C and unchanged even though the sintering temperature was further increased. The emission peak in the green region was similar with the single emission band of ZnO, while that in the orange region was related to the long-lasting phosphorescence.

Kim *et al.* (2007) [58] investigated the changes in the characteristics of ZnO-coated MgO nanowires resulting from application of a thermal annealing process. Thermal annealing affected the structural morphology contributing to an agglomeration of particle-like structures coated on ZnO shell. The SEM images showed the ZnO structures increased in size as a result of the thermal annealing process. TEM images showed the amorphous ZnO shell. While the ZnO coating changed the shape of PL spectrum by inducing UV and green emissions, the relative green emission intensity compared to the UV emission intensity in the case of annealed core/shell structures was higher than that of as-synthesized structures. This was tentatively attributed to an increase in the amount of oxygen vacancies as a result of the thermal annealing.

Qin *et al.* (2007) [59] synthesized an urchin-like ZnO/MgO hierarchical structure via the single-step of thermal evaporation in the mixture of metal Zn and Mg powders under designed conditions. The morphology observations, structure analysis of ZnO/MgO hierarchical structures, and the related by products revealed a morphology evolution linkage as MgO spheres-ZnO/MgO hierarchical structures-ZnO flowers. The investigations suggested that the temperature and ZnO_x concentration in gas flow played a crucial role in the formation of these structures, especially for the hierarchical structure. The photoluminescence (PL) spectra showed that the morphology evolution of the products accompanied changes in the emission characteristics of the PL spectra.

Zhuang *et al.* (2008) [60] reported that the single-phase epitaxial $Mg_xZn_{1-x}O$

(0.4 bxb 0.9) alloy films with wide band gap were deposited on cubic $LaAlO_3$ (LAO) (100) substrates by pulsed laser deposition (PLD). X-ray diffraction measurement and TEM photograph indicated that the cubic phase were stabilized up to Zn content about 0.6 without any phase separation. The lattice parameters *a* of $Mg_xZn_{1-x}O$ films increased almost linearly with increasing ZnO composition, while the band gap energy of the materials increased from 5.17 to 5.27 eV by alloying with more MgO. The cross section morphology revealed the layer thickness about 250-300 nm and AFM scan over a 30 μm by 30 μm area revealing a surface roughness (R_a) about 100 nm. These films were employed for fabrication of heterostructures for actual applications.

Hng *et al.* (2008) [61] studied the effects of MgO (0-40 mol%) on the microstructure and the electrical properties in a binary ZnO-0.5 mol% V_2O_5 system. The microstructure of the samples consisted mainly of ZnO grains with MgO and g-$Zn_3(VO_4)_2$ as the minority secondary phases. MgO was found to be effective as a grain growth inhibitor in controlling the ZnO grain growth, and a more uniform microstructure was obtained. The non-linear coefficient value was found to increase with the amount of MgO, and the highest value of 8.7 was obtained for the sample doped with 10 mol% MgO.

Chawla *et al.* (2008) [4] reported that ZnO and its ternary alloy ZnMgO offered an excellent material system with potential in applications related to quantum well with photonic devices in UV and visible. ZnO and ZnO/MgO composite were also prepared by solid-state mixing and sintered at high temperature in reducing atmosphere. ZnO/MgO nanocomposites up to 50% Mg content could be prepared in the same procedure. X-ray diffraction showed hexagonal of ZnO structure with small signature of a cubic phase of MgO, which increased with increasing the Mg content. The average crystallite sizes calculated from the Scherrer equation were approximately 40 nm. The photoluminescence (PL) studies revealed excitation peak around 290 nm (4.3 eV) and 350 nm (3.5 eV). Pure ZnO nanophosphor showed emission peak around 508 nm, revealing the blue shifted with increasing Mg content. Time resolved decay of PL indicated a decay time in the microsecond time scale. Optical absorption spectra showed the bandgap about 5.6 eV for ZnO/MgO nanocomposite with 50% Mg content. The optical absorption measurement was done in the colloidal suspension. It was expected that the nanoparticles formed very small grain size were effectively contributed to the optical absorption process. The large bandgap was then manifestation of a quantum size effect.

Geng *et al.* (2008) [62] synthesized $(MgO)_x(ZnO)_{1-x}$ materials using mesoporous carbon as a template. With increasing of the MgO content in the materials greater than 25%, the $(MgO)_x(ZnO)_{1-x}$ materials began to form the mesoporous structure. In photoluminescence spectra, all samples except pure ZnO showed both the band-edge emission and the deep-level emission (green band). It was interested to note that the UV emission peak energy (E_{UV}) had a red-shift of about 48 meV at a low MgO content range of 0-25%, while when the MgO content varied from 25 to 75%, the E_{UV} displayed a blue-shift of about 36 meV to the higher energy direction. The optical band gap (E_g) was calculated through linear fitting method. It was found that E_g in this experiment was smaller than that in literature. It can be assumed the trend of mesoporous formation. The mesoporous $(MgO)_x(ZnO)_{1-x}$ materials were expected to have potential application in optoelectronic devices.

Strizhak *et al.* (2008) [63] prepared the ZnO/MgO solids by colloidal technique which involved the deposition of preformed colloidal ZnO nanoparticles on magnesia. The morphology of ZnO nanoparticles was investigated by transmission electron microscopy and UV-Vis absorption and diffuse reflectance spectroscopy. They found a good agreement between the average radius and the particle size distribution of the ZnO nanoparticles obtained by both methods. It was shown the ability to control the size of the supported ZnO nanoparticles (3.8-4.4 nm) by varying the pH of the colloidal solution.

1.7 Objectives of the study

1.7.1 To synthesize pure ZnO and ZnO/MgO nanocomposites by Flame Spray Pyrolysis

1.7.2 To characterize pure ZnO and ZnO/MgO nanocomposites